Multi-Degree-of-Freedom Thin-Film PZT-Actuated Microrobotic Leg

Choong-Ho Rhee, *Member, IEEE*, *Member, ASME*, Jeffrey S. Pulskamp, Ronald G. Polcawich, *Member, IEEE*, and Kenn R. Oldham, *Member, IEEE*, *Member, ASME*

***Abstract*—As a novel approach to future microrobotic locomotion, a multi-degree-of-freedom (m-DoF) microrobotic appendage is presented that generates large range of motion (5°–40°) in multiple axes using thin-film lead zirconate titanate (PZT) actuators. Due to the high driving force of PZT thin films and a robust fabrication process, m-DoF legs that retain acceptable payload capacity (∼2 mg per leg) are achieved. The fabrication process permits thin-film PZT actuator integration with more complex higher aspect ratio silicon structures than previous related processes, using vertical silicon dioxide barrier trenches formed before PZT deposition to provide robust encapsulation of the silicon during later XeF_2 release. Planarization of the barrier trenches avoids detrimental effects on piezoelectric performance from the substrate alteration. Once fabricated, kinematic modeling of compact PZT actuator arrays in prototype leg joints is compared to experimental displacement measurements, demonstrating that piezoelectric actuator and assembled robot leg joint performance can be accurately predicted given certain knowledge of PZT properties and residual stress. Resonant frequencies, associated weight bearing, and power consumption are also obtained. [2012-0041]**

***Index Terms*—Actuators, lead zirconate titanate (PZT), piezoelectric devices, robots.**

I. Introduction

MICROROBOTS are a frequently discussed potential application of the ability to create highly engineered microdevices synthesizing microactuators, sensors, and processing circuitry [1]. Various microactuation mechanisms developed for walking microrobotic locomotion have been reported in the literature, but existing approaches typically feature limited mobility, large power requirements, or low speed. Thin-film piezoelectric actuation, integrated into multi-degree-of-freedom (m-DoF) robot legs may be able to overcome some of these limitations on autonomous microrobots.

Several previous researchers have demonstrated microelectromechanical-systems (MEMS)-based microrobots of less than 1 cm in length using various actuation mechanisms. For example, Ebefors *et al.* built a silicon walking robot with single-degree-of-freedom thermally actuated polyimide leg joints [2]. Although the polyimide joint structures provided large weight-bearing capacity, large power consumption and low speed were a result of thermal actuation. This tradeoff was also demonstrated by Murthy *et al.* [3] and Mohebbi *et al.* [7]. In [4], Hollar *et al.* built the electrostatic inch-worm motors in a two-legged microrobot. However, the pin-joint hinge mechanism provided a single-degree-of-freedom motion, although power consumption was very small. In [5], Bergbreiter and Pister integrated electrostatic inchworm motors with molded elastomers to generate a rapid jumping motion from a similar power source and actuation mechanism as in [4]. In [6], Donald *et al.* used electrostatic scratch drives that were actuated by electric potential difference between the actuator and the substrate, but this type of actuation limits the mobility of the microrobot to a certain operating environment.

Piezoelectric actuation is a desirable candidate technology for microrobotics because it may dramatically increase appendage speed and has large force capacity, modest voltage requirements [16], and ability to recover much stored electrical energy using charge recovery techniques [19]. Recently, lateral thin-film lead zirconate titanate (PZT) actuators were developed in [8] that demonstrated very large work densities and could be connected in parallel or series to provide large force capacities or range of motion, depending on application. Lateral thin-film PZT actuator arrays generating series rotation between 5° and 20° at 20 V potentially enable comparatively large range of motion for autonomous microrobotic appendages [9], [10], while vertical bending piezoelectric actuators can achieve even larger angles.

A first topic of this paper is to introduce basic models of out-of-plane and in-plane piezoelectric actuator arrays for microrobotic leg joints, to illustrate the critical properties of actuator design. The strength of thin-film PZT actuation for microrobotic applications is the combination of high speed, relatively large angle, and low-power operation in multiple axes, as compared to previous technologies in Table I. The cost for this improvement on the various prior robotic leg technologies is a reduction in payload capacity, at least for the type of leg configurations to be discussed in this paper.

The second topic of this paper is a robust fabrication process of the microrobotic leg joints based on thin-film PZT actuator arrays. Integrating large numbers of thin-film piezoelectric actuators into high-performance legs with multiple degrees of freedom requires high-yield fabrication of both vertical and lateral actuators and appropriate connecting structures. Preferably, associated structures should be composed of

Manuscript received February 22, 2012; revised July 3, 2012; accepted July 16, 2012. Date of publication August 27, 2012; date of current version November 27, 2012. This work was supported in part by the U.S. Army Research Laboratory under Award W911QX-07-C-0072 and in part by the National Science Foundation under Award CMMI 0954422. Subject Editor G. Stemme.

C.-H. Rhee and K. R. Oldham are with the Department of Mechanical Engineering, University of Michigan, Ann Arbor, MI 48109 USA (e-mail: chrhee@umich.edu; oldham@umich.edu).

J. S. Pulskamp and R. G. Polcawich are with the Micro and Nano Electronic and Materials Branch, U.S. Army Research Laboratory, Adelphi Laboratory Center, Adelphi, MD 20783 USA (e-mail: jeffrey.s.pulskamp.civ@mail.mil; ronald.g.polcawich.civ@mail.mil).

Digital Object Identifier 10.1109/JMEMS.2012.2211573

TABLE I
COMPARISON OF MICROROBOTIC DEVICES

	Weight Bearing	Speed [mm/s]	DoF	Maximum Angle	Volt	Power Consumption
Ebefors (Thermal)	312.5 mg/leg	6	1	~18.7°	18V	1.1W
Hollar (Electrostatic)	5.1 mg/leg	4	1	35°	50V	100nW
Murthy (Thermal)	667 mg/leg	1.55	1	~2.9°	10V	750mW
Mohebbi (Thermal)	1448 mg	0.64	3	N.A.	60V	Not specified
Current Work (Piezoelectric)	2.1 mg/leg	27 (est. max.)	3	5°, 40°	18V	60μW

high-aspect-ratio silicon or other hard materials to maintain weight-bearing capacity.

Previous processing techniques for integrating thin-film PZT unimorph benders with high-aspect-ratio structures have limited the complexity of potential microactuator joint arrays. Conway and Kim demonstrated an SU-8 integrated amplifying mechanism in [17]. Although SU-8 could be chosen for potential microactuator joint arrays, it is limited to single-level processing above the piezoelectric film. In another work, Aktakka *et al.* developed a multilayer PZT stacking process over high-aspect-ratio structures in [18]. Although the thickness of a thinning-stop layer could be chosen for various target thicknesses of the resulting PZT layer, this PZT remains thick compared to chemical-solution-deposited thin-film PZT and thus requires large voltages for equivalent strains. For several energy-harvesting devices, such as that in [20], silicon is left underneath the thin-film PZT layer; this can be acceptable for energy harvesting from vibration at such devices' natural frequency, even under the environmental vibration at low frequency. However, timed wet etching used to obtain the silicon cantilever is not desirable for undercutting the PZT layer itself, which limits displacement as an actuator.

To overcome previous processing limitations for producing complex microrobotic joint structures, low-pressure chemical vapor deposition (LPCVD) of silicon oxide vertical barrier trenches prior to thin-film PZT deposition was performed in this paper. Compared to a previous photoresist encapsulation technique in [11], consistent undercut length of thin-film PZT actuator array was realized that is essential for producing the proposed microrobotic platforms with complex joint configurations. An effective piezoelectric strain coefficient is obtained with minimal change in magnitude from PZT structures without the barrier trenches.

The final topic of this paper is then a description of experimental testing procedures and measured robot leg behavior, as related to range of motion, response speed, and power consumption. After fabrication, a prototype leg joint is characterized experimentally to validate the in-plane and out-of-plane joint models. Important nonidealities of the fabrication process as they influence robot leg joint performance and appropriate adjustments to displacement models described are noted.

To summarize paper organization, Section II introduces the analytical models for piezoelectric vertical and lateral actuators and applies them to the actuator arrays produced in this paper. Section III describes the fabrication process for thin-film piezoelectric layer, integrated with complex silicon microrobotic structures. Section IV presents experimental characterization of fabrication process and of the kinematics and dynamics of a sample microrobotic leg. Section V concludes this paper.

II. System Description

A. Thin-Film PZT Actuator Basics

Two types of thin-film piezoelectric actuators are used to create M-DoF appendages such as that shown in Fig. 1: lateral (or in-plane) rotational actuators and vertical (or out-of-plane) unimorph bending actuators [15]. Individual thin-film PZT actuators consist of unimorph bending segments, as in [8]: a single bend-down uniform segment for the vertical actuators and a combination of two bend-down and two bend-up segments for the lateral actuators. Each segment contains a material stack of a base silicon dioxide layer, a bottom Ti/Pt electrode, the PZT thin film, and a top Pt electrode. For bend-down segments, an additional gold film is deposited to move the neutral axis of the unimorph above the centerline of the PZT film, as shown in Fig. 2. In the material stack, the PZT thin film both imposes a contractive force F_{act} and a bend-down or bend-up moment $M_{\mathrm{act},1}$ or $M_{\mathrm{act},2}$, under an applied voltage according to

$$F_{\mathrm{act}} = e_{31,\mathrm{eff}} \frac{V}{t_{\mathrm{PZT}}} A_{\mathrm{PZT}} \tag{1}$$

$$M_{\mathrm{act,i}} = e_{31,\mathrm{eff}} \frac{V}{t_{\mathrm{PZT}}} A_{\mathrm{PZT}} (\overline{y}_{\mathrm{PZT}} - \overline{y}_i) \tag{2}$$

where $e_{31,\mathrm{eff}}$ is the effective field-dependent electroactive stress coefficient, which is a measured ratio of stress to electric field rather than the exact linear piezoelectric coefficient of the material [8]. The coefficient is approximated by the nominal (short circuit) axial elastic modulus E_{PZT} of the PZT film in a free beam and by the effective field-dependent electroactive strain coefficient $d_{31,\mathrm{eff}}$ or $e_{31,\mathrm{eff}} = E_{\mathrm{PZT}} d_{31,\mathrm{eff}}$. The empirical values of $e_{31,\mathrm{eff}}$ and $d_{31,\mathrm{eff}}$ include a number of effects associated with the effective piezoelectric coefficient $d_{31,f}$ or effective piezoelectric stress coefficient $e_{31,f}$ but also nonlinear piezoelectric/ferroelectric and electroactive material responses [11]. For other nomenclature, V is the applied voltage, t_{pzt} and A_{pzt} are the thickness and the cross-sectional area of PZT, $\overline{y}_{\mathrm{PZT}}$ is the position of the PZT film midline in the unimorph material stack, and $\overline{y}_1$ and $\overline{y}_2$ are neutral axes of segments with (bend down) and without (bend up) a gold layer. The composite rigidity of respective thin-film PZT unimorphs is referred to as $(EI)_1$ or $(EI)_2$. The aforementioned parameters associated with thin-film PZT actuator structure are shown in Table II.

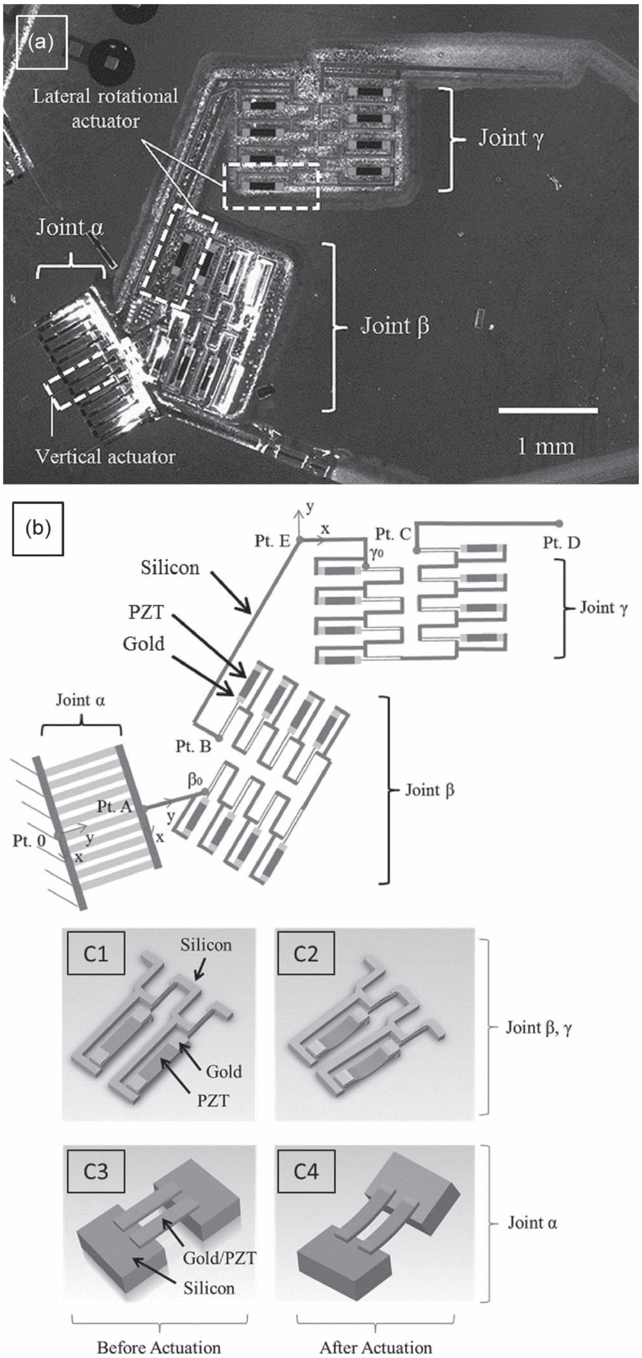

Fig. 1. Fully released m-DoF leg. (a) Optical image. (b) Schematic drawing. (c) Schematic drawing of actuation substructures [(left) before actuation, (bottom left) before actuation of PZT film, and (bottom right) after actuation of PZT film].

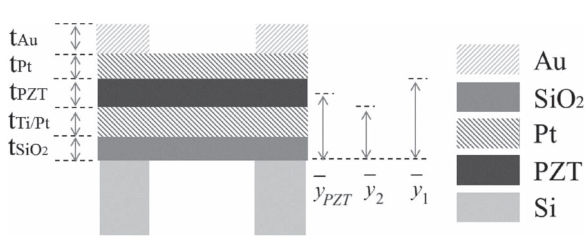

Fig. 2. Cross-sectional view of a lateral rotational actuator.

TABLE II
PROPERTIES OF THIN-FILM PZT LATERAL ROTATIONAL AND VERTICAL ACTUATORS

Parameter	Value	Parameter	Value
t_{Au}	1 (μm)	L_{PZT}	480 (μm)
t_{Pt}	0.105 (μm)	L_v	536 (μm)
t_{PZT}	0.8 (μm)	$w_{flexure}$	13 (μm)
$t_{Ti/Pt}$	0.08 (μm)	w_{tether}	10 (μm)
t_{SiO2}	0.17 (μm)	$(EI)_{\text{flex}}$	$1.693\cdot10^2$ (N·μm²)
$\bar{y}_{PZT}$	0.62 (μm)	$(EA)_{\text{t}}$	11.20 (N)
$\bar{y}_1$	1.05 (μm)	$(EI)_1$	6.909 (N·μm²)
$\bar{y}_2$	0.32 (μm)	$(EI)_2$	1.986 (N·μm²)
L_{flex}	118 (μm)	F_{act} (at 20V)	$1.17\cdot10^{-2}$ (N)
L_{tether}	284 (μm)	$M_{act,1}$(at 20V)	$5.3\cdot10^{-2}$ (N·μm)
L_{act}	15.5 (μm)	$M_{act,2}$ (at 20V)	$3.7\cdot10^{-2}$ (N·μm)

B. Thin-Film PZT Vertical Actuator Array

Out-of-plane motion is generated by simple unimorph bending in the first joint (joint α) of the m-DoF appendages shown in Fig. 1(a) and (b). Displacements of any actuator array can be expressed using six coordinates, $d = [x\ y\ z\ \theta_x\ \theta_y\ \theta_z]^{\mathrm{T}}$, although only specific coordinates of significant motion are shown in each respective joint analysis. Since all out-of-plane or vertical actuators are composed of identical silicon dioxide, PZT thin film, and metal layers, a multilayer composite cantilever is an appropriate model to estimate the displacement of vertical actuator $d_{(\alpha)}$

$$d_{(\alpha)} = \begin{bmatrix} z_{(\alpha)} \\ \theta_{x,(\alpha)} \end{bmatrix} = \begin{bmatrix} \frac{L_v^2}{2(EI)_1} \\ \frac{L_v}{(EI)_1} \end{bmatrix} M_{\text{act},1} + \begin{bmatrix} \frac{L_v^3}{3(EI)_1} & \frac{L_v^2}{2(EI)_1} \\ \frac{L_v^2}{2(EI)_1} & \frac{L_v}{(EI)_1} \end{bmatrix} \begin{bmatrix} \frac{F_v}{N} \\ \frac{M_v}{N} \end{bmatrix} \quad (3)$$

where $z_{(\alpha)}$ and $\theta_{x,(\alpha)}$ are the vertical displacement and the rotational angle at the tip of joint α, L_v is the length of a vertical actuator, F_v and M_v are external force and moment, if present, due to the external loads applied at the tip of vertical actuators, and N is the number of vertical actuators connected in parallel. A schematic view of this motion is shown at the bottom of Fig. 1(c). If desired, a lateral displacement at the tip of the joint $y_{(\alpha)}$ component may also be estimated through numerical integration along the small angle displacement of $\theta_{x,(\alpha)}$. In prototype leg joints, ten vertical actuators are connected in parallel such that large weight-bearing capability can be maintained by joint α.

As implied by (2) and (3), vertical actuator joint angles can be very large when using thin-film PZT unsupported by silicon because the effective piezoelectric coefficient is relatively large, electric fields are high, and composite stiffness is low. Downward bending motion is used, with the added gold layer of bend-down unimorphs both increasing offset from the PZT layer to the neutral axis and preventing composite stiffness of the beams from becoming too low in resisting external loads.

C. Thin-Film PZT Lateral Rotational Actuators

In-plane motion is driven by individual lateral PZT actuators [21], [22] integrated with silicon flexural structures. The

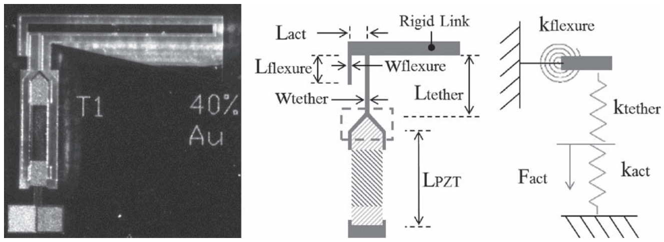

Fig. 3. Single thin-film PZT lateral rotational actuator connected to a high-aspect-ratio silicon flexural structure. (Left) Optical image. (Center) Schematic drawing. (Right) Equivalent spring structure. (Dashed-line box) Outline of the detailed view given in Fig. 6.

net motion at the tip of individual lateral actuators is ideally horizontal, as two bend-down and two bend-up segments are located symmetrically on either side of the actuator midpoint. However, due to residual stress in the thin films, unconstrained in-plane motion is not generally obtained. Thus, the end of the actuator is connected to a high-aspect-ratio silicon flexural structure that prevents out-of-plane bending under most circumstances. The flexure structure also converts small translational piezoelectric displacements into rotational displacements, as shown in Fig. 3.

Force–displacement curves for such lateral actuators have been previously described in [8]. For microrobotic leg design, a region of small displacement and large force is chosen to increase the weight-bearing capacity and locomotion speed of joint structures. In that region of behavior, the axial contraction in (1) dominates actuator motion, while the bending motion of beams that can lead to larger displacements against small forces has negligible influence on the present leg joint designs. Equation (4) shows the in-plane small displacement of a single actuator rotary joint that consists of high-aspect-ratio elastic flexure and tether, a PZT actuator, and a rigid link. The relation of the force generated by a single actuator and the displacement at the tip of the flexure in the rotary motion is as follows:

$$\left(\frac{k_{f,\theta}k_{t,\theta}}{k_{f,\theta}+k_{t,\theta}}+k_{\mathrm{act},\theta}\right)\theta=F_{\mathrm{act}}L_{\mathrm{act}} \tag{4}$$

where $k_{f,\theta}$, $k_{t,\theta}$, and $k_{\mathrm{act},\theta}$ are the equivalent rotational spring stiffness values of the flexure, tether, and actuator, which are given in the Appendix. L_{act} is the distance between the tether and the flexure joint. Because the actuator itself and the silicon tether experience the axial force generated by piezoelectric film, the maximum rotary angle θ is represented in terms of the combined spring stiffness of the joint structure.

D. Thin-Film PZT Lateral Actuator Arrays

For intended in-plane actuation in microrobotic legs, multiple lateral actuators are connected in series arrays so that large rotational displacement can be produced. In the prototype legs, this occurs in joints β and γ. In these joints, lateral actuators are arranged in two sets of four with flexural mechanisms facing each other, as shown in Fig. 1(b). A schematic view of this motion is shown in Fig. 1(c). By aligning the high-aspect-ratio flexures toward a microrobot's foot, such arrays are intended to reduce out-of-plane deflection due to torsion from weight bearing of future microrobotic platforms and to multiply rotational motion of individual actuators.

Within each in-plane joint array, displacement is calculated from the driving thin-film PZT actuation force and its equivalent rotary moment. Eight local coordinates, as shown in Fig. 4, are used to calculate the total displacement. The displacement of the origin of the ith coordinate with respect to the first coordinate at the start of the array (point β_0 or γ_0) is represented as the summation of projections onto previous coordinates. Then, displacement of the mth coordinate with respect to the origin of the first flexure joint is represented in

$$d^1_{m(\beta,\gamma)}=\sum_{n=1}^{m}\prod_{k=1}^{n}R^{k-1}_{k\ (\beta,\gamma)}\left(p^n+T\cdot f^n_{(\beta,\gamma)}+R^n_{n+1(\beta,\gamma)}q^{n+1}\right) \tag{5}$$

where $d^1_{8\ (\beta,\gamma)}$ is the total local displacement of the compact array in question, R^j_i is the rotational matrix of the ith coordinate with respect to jth coordinate by the angle of θ_i, and, for $i \geq 5$, R^4_i is a combined transformation of the reorientation of axis by π radians $R(\pi)$ with rotational displacement by $\theta_i R(\theta_i)$. When $i = 1$, R^0_1 is the identity matrix. T is the compliance matrix of the flexure structure, f^i is the forcing term generated by the actuator and, if present, external forces and moments, p^i is the initial position of flexure tip, and q^i is the position vector between the ith and $i-1$th coordinates. The subscript β or γ indicates whether the model is referring to the inner or outer compact array.

For in-plane actuator design, performance is best if the elastic flexure, denoted by $k_{f,\theta}$, can be fabricated with high aspect ratio, so that out-of-plane stiffness and weight bearing are increased without overly increasing resistance to in-plane motion. Likewise, small gaps between flexures and tethers L_{act} are also useful for generating large rotation angles. Significant forcing is again available through large piezoelectric coefficient and high electric field across the PZT thin film.

E. Kinematic Leg Model

In the prototype leg configuration, coordinate systems are defined at the silicon flexures of each individual in-plane actuator, in addition to the initial vertical actuator. As shown in Fig. 1, the following locations are used as reference frame of the local coordinates during kinematic analysis.

1) Point 0 represents the beginning of leg, at the fixed end of the vertical actuators, oriented along the long axis of the vertical actuators.
2) Point A represents the tip of the vertical actuators (end of joint α), where a rigid silicon connection to joint β begins.
3) Points β_0 and B represent the beginning and end of joint β, at the end of the rigid silicon connector between joints α and β.
4) Points γ_0 and C represent the beginning and end, respectively, of joint γ, at the end of the rigid silicon connector between joints β and γ.
5) Point D is the end tip of the m-DoF leg.

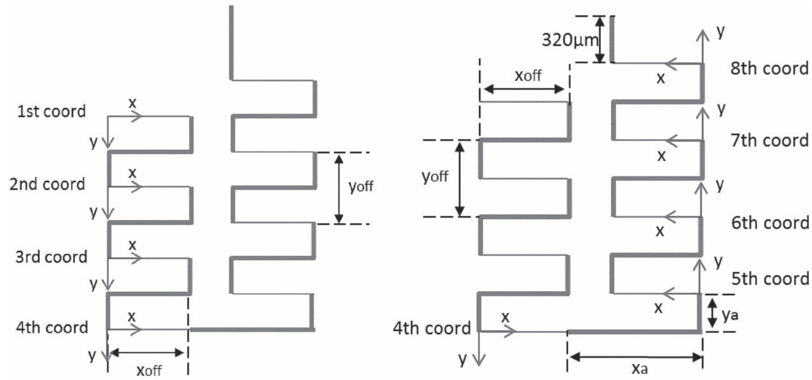

Fig. 4. Schematics of local coordinates of inner and outer actuator array in m-DoF robotic leg.

6) Point E is the corner of the rigid silicon link between joints β and γ, which is easily tracked during experimental measurements.

The local coordinate axes for each joint is chosen such that the y_0-axis is aligned along the lateral direction of the thin-film PZT actuators in the given joint. Local displacements are related to global displacements of points of interest using rotation matrices. Fixed rotation matrices are denoted by the notation $R(\theta_{i,b/a})$, where i corresponds to the local axis of rotation and b and a indicate the ending and starting points of interest, respectively, that a change in orientation is taken from. As an example, for the first rotation matrix, from the global coordinates to the base of the vertical actuators, the rotational matrix is formed from $\theta_{z,A/0}$ which is the angle between global coordinates $(x_{\text{global}}, y_{\text{global}}, z_{\text{global}})$ and the local coordinates (x_0, y_0, z_0) at point 0, the beginning of the leg. From the measured distance of point A from zero, $\theta_{z,A/0}$ is estimated at 39.5°, and coordinate transformation from the raw data to the desired coordinate (x_0, y_0, z_0) is obtained in

$$X_{\text{global}} = R(\theta_{z,A/0})X_0 \tag{6}$$

where X_{global} and X_0 are the position vectors with respect to the global and point 0 coordinates.

Rotations that may change with applied voltage are also written using standard rotation matrices, denoted by $H(\theta_{i,b/a})$, and generally, their rotation angles consist of a fixed component, due to residual stress, and a changing component due to applied voltage. For example, the rotation matrix used to transform coordinates about point A with respect to coordinates about point 0 is written $H(\theta_{x,A/0})$, with $\theta_{x,A/0}$ being the sum of vertical rotations at the tip joint α due to residual stress and due to an applied input voltage. Use of these rotations to evaluate leg joint performance will be discussed in more detail in Section IV.

III. Fabrication

A. Robust Encapsulation and Multilevel Fabrication Integrated With Thin-Film PZT Layer

A previous microfabrication process for components of thin-film PZT-actuated microrobotic leg joints has been reported in [8]. Individual actuators were released from underlying silicon with a timed XeF_2 etch when a photoresist encapsulation layer protects silicon anchor points. However, this resulted in obstacles to releasing the undercut PZT actuator layer across large devices, such as inconsistent actuator undercut length and occasional crack and failure of photoresist encapsulation layer.

A robust fabrication process used to produce the current m-DoF appendages is as follows. Fabrication begins with a silicon-on-insulator (SOI) wafer with a 10-μm-thick device layer, 0.1-μm-thick buried oxide layer, and 500-μm-thick handle wafer (thicker device layers may also be used, with legs from 30-μm device layers also fabricated). Narrow (3 μm wide) trenches are etched to the buried silicon dioxide layer (step A) in Fig. 5) along the sidewalls of bulk-micromachined silicon structures, such as flexural springs and silicon connectors from the tethers to PZT unimorphs. Prefurnace-cleaned trenches are then filled with silicon dioxide by LPCVD [step B)].

It was observed that keyholes are generated in the oxide trenches due to nonuniformity in the trench sidewalls and a slightly faster deposition rate at the trench mouth than that inside the trench. Instead of annealing above 1000 °C, which has been shown to make the oxide reflow in the trench [12], the top oxide is removed by either chemical mechanical polishing or reactive ion etching (RIE), and the upper part of the trench is etched by short RIE [steps C) and D)]. Once the keyhole is opened, LPCVD process is repeated to fill the opened trenches in step E). Several iterations of steps B)–D) may be necessary to diminish the size of keyhole, but it is difficult to eliminate it entirely. Nonetheless, since the observed piezoelectric coefficients of PZT films can be very sensitive to underlying surface conditions [13], refill is continued until a standard mechanical boundary condition of the intermediate layer between PZT film and the substrate is achieved. In this case, closure of all surface trenches and a planarized surface are achieved. Planarization of the surface of refilled oxide trenches is followed by additional silicon dioxide deposition by plasma-enhanced chemical vapor deposition to reach a minimum target base oxide thickness of 2000 Å.

After SOI wafers are processed up to step E), PZT (with a Zr/Ti ratio of 52/48) and electrode layers are deposited at the U.S. Army Research Laboratory and Radiant Technologies, Inc. The resulting metal stack consists of a platinum bottom electrode, PZT film, and platinum top electrode [step F)]. Two argon milling steps for the top electrode and PZT layers and

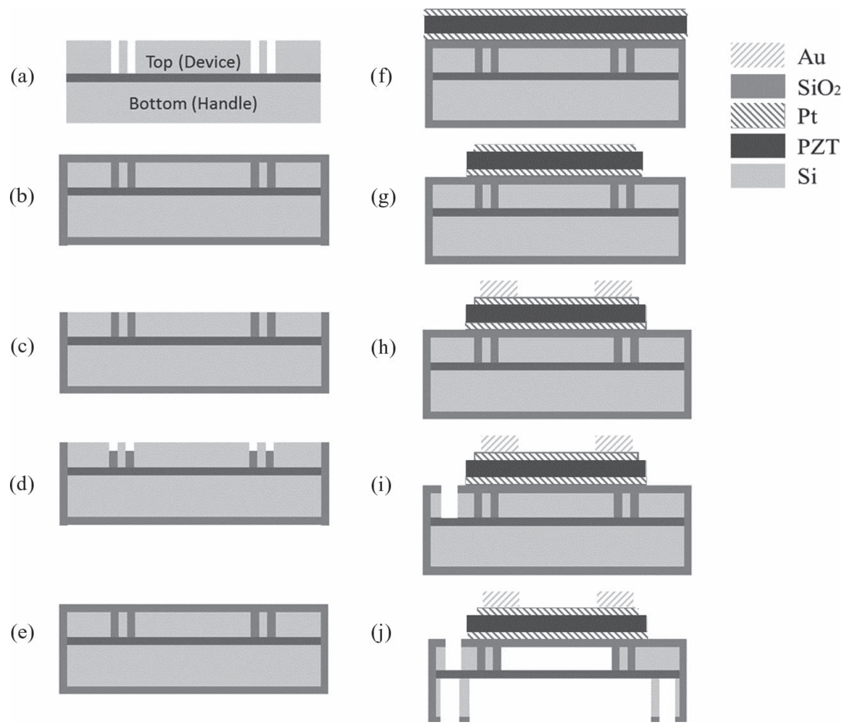

Fig. 5. Multilevel microfabrication process flow of thin-film PZT-actuated silicon structure in the microrobotic application.

a wet etch for contact vias to the bottom electrode are next performed [step G)], as in [8]. Then, a 1-μm-thick Ti/Au layer is deposited on the top of PZT actuator surface by a lift-off process [step H)], and the silicon microstructure in the top device layer is patterned and micromachined by deep RIE (DRIE) [step I)].

To perform backside etching of the SOI wafer, oven-baked photoresist is used to protect the microstructure of top device layer, and the backside of SOI wafer is patterned for other geometries such as microrobot feet. Backside patterning and etching also provide the open area for XeF_2 to etch the underneath silicon layer of actuator and other unprotected silicon structures in step J). During the XeF_2 underetching process of thin-film PZT actuator and silicon microstructure layer, a uniform undercut length of the PZT/Au unimorph actuator structure is obtained after removal of chemically inert Teflon-like passivation layer, which is deposited during DRIE process and prevents XeF_2 gas from etching the silicon underneath the material stack. Fig. 6 shows a scanning electron microscopic image of thin-film PZT actuator layer connected to silicon tether.

To summarize, in the microfabrication process described earlier, deposition of oxide trenches provides a vertical etching barrier against isotropic XeF_2 etching of the substrate silicon device layer connected to thin-film PZT actuators. This serves as a robust encapsulation structure to eliminate encapsulation failures and underetching variance of thin-film PZT actuators observed in previous integration approaches. Oxide deposited for such trenches can also be used as a hard mask on the backside of a SOI wafer permitting backside patterning and thus multilevel fabrication for complex silicon structure. Silicon structures up to 30 μm tall by 5 μm wide have been produced in this manner on other test wafers.

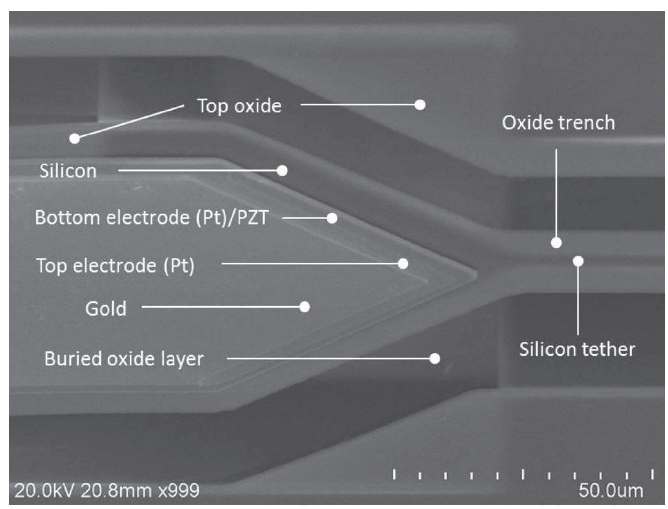

Fig. 6. Scanning electron microscopic image of thin-film PZT actuator layers connected to silicon tether, as marked in a dashed red box in Fig. 2.

One limitation of the finalized process flow is an inability to remove the oxide trenches following XeF_2 release. While the oxide trenches were originally intended to be removed via isotropic RIE, and structures were designed with the removal of silicon dioxide expected, in practice, the top platinum electrode on the PZT layer was found to be eroded in such an RIE step, causing the removal of electrical connection in most of actuators. Thus, flexible structures in the device layer are wider than originally designed by the oxide trench width, and flexible electrical interconnects (such as that providing power to the outer in-plane actuator) are also reinforced. This reduces the range of motion of the final leg structures compared to their designed specifications, and future devices should take oxide trench width into account in the design stage. In addition, residual stresses in the metal stack result in the vertical actuator array having a nonzero neutral position. The change of the neutral position leads to variation in vertical displacements from planar neutral position which would be expected from an initially flat structure.

IV. Experimental Results

A. Piezoelectric Coefficient Measurement

Following fabrication, simple cantilever beams were used to verify piezoelectric coefficient magnitudes. This was done to verify that the preprocessing of the SOI with barrier trenches would not have a detrimental effect on thin-film PZT quality. Since a randomly oriented polycrystalline structure is present in PZT thin film after fabrication, a poling treatment is required to align the scattered polydomain structure into a metastable alignment in the direction of an applied electric field to form a consistent remnant polarization of the layer. The poling test was performed at 250 kV/cm (i.e., 20 V) using a direct-current power supply at room temperature which was used for 45 min. After poling, the static vertical displacement of the tip of cantilever was measured by optical profilometry by stepping down to 0 V in 1-V decrements and returning back to 20 V in 1-V increments.

Due to intrinsic residual thin-film stress following fabrication, the piezoelectric coefficient is experimentally determined from radius of curvature of the beam ρ in the Bernoulli–Euler equation with the superposition of the resultant moment due to the residual stress and the moment generated by PZT thin film

$$\frac{1}{\rho} = -\frac{M_{\text{residual}} + M_{\text{PZT}}}{(EI)_{\text{comp,no Au}}} \tag{7}$$

$$M_{\text{PZT}} = e_{31,\text{eff}} \frac{V}{t_{\text{PZT}}} A_{\text{PZT}} (\bar{y}_{\text{PZT}} - \bar{y}_1) \tag{8}$$

where M_{residual} is the moment due to residual stress of the films, M_{PZT} is the moment generated by PZT actuator, which corresponds to $M_{\text{act},2}$ in (2), and $(EI)_{\text{comp,no Au}}$ is the vertical composite rigidity of the material stack without Au deposition. Fig. 7 shows the estimated field-dependent effective electroactive strain coefficient $d_{31,\text{eff}}$ of the piezoelectric cantilevers with and without oxide barrier trenches. Multiple measurements have been performed at each applied electric field and represented as error bars, and the electroactive $-d_{31,\text{eff}}$ values for both test cantilevers at higher voltages are determined in the range of 60–80 pm/V. The variation of measured $d_{31,\text{eff}}$ with respect to electric field is observed inversely proportional to the applied electric field as deflection due to intrinsic residual stress is predominant at low voltage and the piezoelectric coefficient is inversely proportional to electric field. The empirical $d_{31,\text{eff}}$ coefficients in Fig. 7 show that the performance of fabricated actuators could be preserved in the proposed microfabrication process, particularly at high voltages where typical operation occurs.

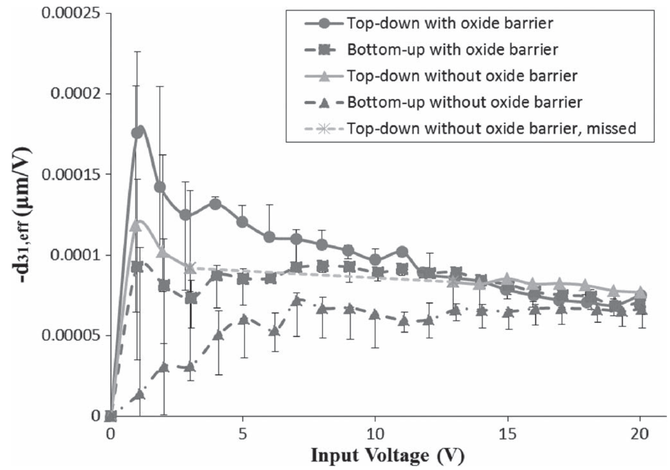

Fig. 7. Empirical effective electroactive piezoelectric strain coefficient curve at applied voltages.

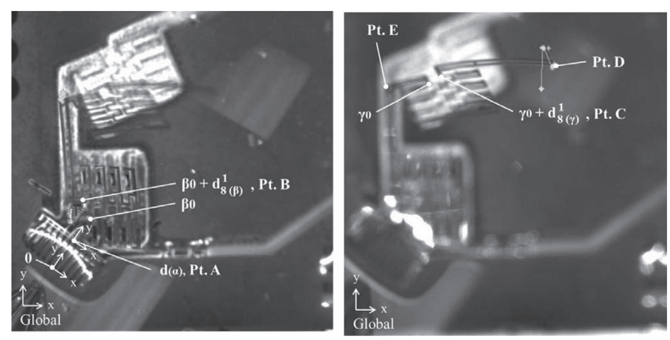

Fig. 8. Trajectory of point E (knee) between joints β and γ and point D (foot) as the vertical actuators are activated by 15-V dc. The left images are at 0 V, and the right images are at 15 V.

B. Range-of-Motion Analysis

Completed m-DoF leg joints were characterized experimentally to verify functionality and vertical and lateral joint design performance. This experimental verification is based on kinematic descriptions of joint motion, with deformation of continuous beams (vertical unimorph actuators and elastic rotational flexures, for out-of-plane and in-plane motions, respectively) converted to motion of specified points on a prototype actuator in global coordinates [14]. This motion was captured by a high-speed camera above the device, and the global coordinate $(x_{\text{global}}, y_{\text{global}})$ data are obtained from the optical images.

As discussed in (6) in Section II-E, displacements of any point of interest, as measured in global coordinates, can likewise be related to rotations and displacements of proceeding links in the robotic leg. For example, the displacement of the tip in terms of global coordinates X_D depends on all relevant rotations and displacements, as

$$\begin{aligned} X_D = {} & H(\theta_{x,A/0}) R\left(\theta_{z,\beta_0/A}\right) H\left(\theta_{x,B/\beta_0}\right) H\left(\theta_{z,C/\gamma_0}\right) X_{\frac{D}{C}} \\ & + H(\theta_{x,A/0}) R\left(\theta_{z,\beta_0/A}\right) H\left(\theta_{x,B/\beta_0}\right) s_{\text{trans}} \\ & + H(\theta_{x,A/0}) R\left(\theta_{z,\beta_0/A}\right) w_{\text{trans}} + H(\theta_{x,A/0}) u_{\text{trans}} \\ & + v_{\text{trans}} \end{aligned} \tag{9}$$

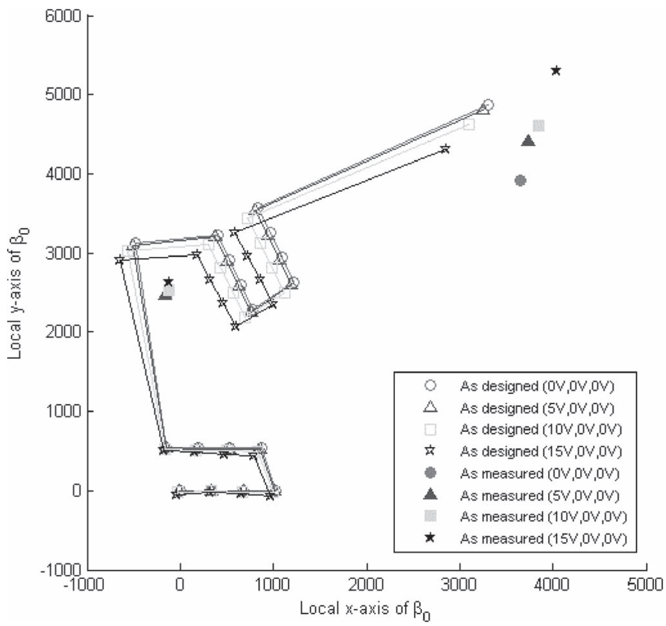

Fig. 9. Trajectory of two in-plane compact arrays with points D (foot) and E (knee) represented with hollow markers, as designed, and represented with solid markers, as measured, with respect to point β_0 when joint α is activated.

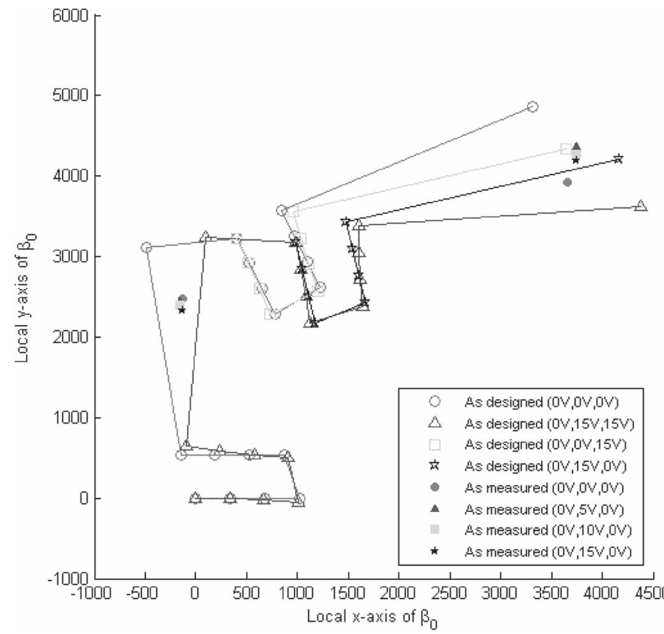

Fig. 10. Trajectory of two in-plane compact arrays with points D (foot) and E (knee) represented with hollow markers, as designed, when joints β and γ are activated separately, and represented with solid markers, as measured, with respect to point β_0 when joint β is activated.

where $H(\theta_{x,A/0})$, $H(\theta_{x,B/\beta 0})$, and $H(\theta_{z,C/\gamma 0})$ are the local coordinate transformations due to rotations at joints α, β, and γ, respectively, and $R(\theta_{z,\beta 0/A})$ is a fixed rotation representing the difference in orientation between joint α and joint β. $X_{D/C}$ is fixed translational offset of the tip of the leg from the end of joint γ, s_{trans} is the nominal offset from the beginning of joint γ to the end of joint γ plus any displacement of joint γ (i.e., $d^1_{8\ (\gamma)}$) due to an applied voltage, w_{trans} is the nominal offset from the beginning of joint β to the end of joint γ plus any displacement exerted by joint β (i.e., $d^1_{8\ (\beta)}$), due to applied voltage, u_{trans} is the nominal offset of joint β from joint α, and v_{trans} is the nominal offset from the beginning to the end of joint α plus any displacement of joint α due to an applied voltage.

Fig. 8 shows the top view of the device and the trajectory of E (knee) and point D (foot) taken by stereoscope and high-speed camera when the vertical actuators are activated by various input voltages. In Fig. 9, the direction of motion of points D and E exerted by joint α is opposite to the intended direction. This is because residual stress causes the leg to start in an upward deflected position, such that downward rotation of the vertical actuator under an applied voltage causes the tip of the leg to move away from the base (in global (x, y) coordinates), rather than closer to the base if the leg had started in a flat fully extended position. Furthermore, residual stress leading to the deformation of joint β causes significant out-of-plane bending.

Fig. 10 shows the measured trajectories of points D and E under various combinations of applied voltage to joints β and γ. Differences between the designed and the measured trajectories of the leg also arise from nonidealities in the fabrication process, particularly the following: 1) excess silicon dioxide that increases the stiffness of flexures and, particularly, the interconnect across the inner lateral actuator and 2) residual stress in the actuator arrays.

TABLE III
DISPLACEMENT OF POINT A BY VERTICAL ACTUATORS

Degree of Freedom	As designed	As fabricated (from model)	As fabricated (from experiment)
x (μm)	0	0	1.86
y (μm)	-43	10.6	19.4
z (μm)	-189	-189	-148
θ_x(°)	-40	-40	-37
θ_y(°)	0	0	0
θ_z(°)	0	0	0

C. Comparison to Actuator Models

Mapping back observed motion at the points of interest along the leg to displacements at the actuator arrays allows the actuator array performance to be measured. Since the motion of m-DoF microrobotic legs is generated by combinations of two in-plane compact actuators and vertical actuators, different sets of actuators were independently activated to verify actuator models. Three sets of displacements are shown in Tables III–V, for the three actuators. The first set of results shows the displacement of an ideal leg design, which assumes a planar neutral position (no residual stress), no excess silicon dioxide, and negligible interconnect stiffness across the inner lateral actuator; this set of results is intended to demonstrate the ideal capabilities of the device. The second set of results shows the predicted displacements when residual stress effects are included, with extra oxide and with full interconnect modeling. The third set of results is from the experimentally extracted actuator array displacements and rotations, when measurable.

TABLE IV
DISPLACEMENT OF POINT E WITH RESPECT TO POINT A BY INNER COMPACT ACTUATORS

Degree of Freedom	As designed	As fabricated (from model)	As fabricated (from experiment)
x (μm)	230	4.9	3.8
y (μm)	65	-133	-143
z (μm)	0	843	798
θ_x (°)	0	18.9	18.1
θ_y (°)	0	0	Unable to measure
θ_z (°)	-4.7	-0.1	-0.1

TABLE V
DISPLACEMENT OF POINT C WITH RESPECT TO POINT E BY OUTER COMPACT ACTUATORS

Degree of Freedom	As designed	As fabricated (from model)	As fabricated (from experiment)
x (μm)	149	144	114
y (μm)	-208	-201	-186
z (μm)	0	0	108
θ_x (°)	0	0	17.7
θ_y (°)	0	0	Unable to measure
θ_z (°)	-4.7	-4.5	-3.85

Based on experimental observations of fabrication limitations, various adjustments were made to the actuator models. First, it should be noted that, even with high-aspect-ratio flexure and tether structures, residual stress in the experimentally released prototype devices described in Section III still led to out-of-plane bending from the in-plane actuators. Thus, an addition to the lateral actuator model to account for out-of-plane deformation was obtained. This was particularly significant when the elastic interconnect is present, as a deformation similar to buckling is observed.

To account for the stiffness of the PZT interconnect to joint γ across joint β, which impeded lateral rotation in joint β and contributed to out-of-plane bending moment about the x-axis, an expanded model of the lateral actuator array with interconnect was created. Details of the augmented model are included in the Appendix, but in brief, this effect can be estimated by the average offset distance $\varepsilon_{\mathrm{dist}}$ of the beginning of the rigid silicon links between joints β and γ along the local z-direction with respect to point A during the motion. This offset distance and in-plane actuation moment result in out-of-plane deflection and, thus, the resulting angle $\theta_{ic,y}$ of the thin-film PZT interconnect about point A. A lumped spring model is used to estimate the displacement of the parallel structure of the elastic interconnect and joint β, which is represented by the displacement of joint $\beta d^1_{8\ (\beta)}$

$$d^1_{8(\beta)} \approx (K_{\mathrm{ic,eq}} G_{\mathrm{ic}} + K_{\mathrm{array,eq}})^{-1} F_{\mathrm{act}} \tag{10}$$

where $K_{\mathrm{ic,eq}}$ and $K_{\mathrm{array,eq}}$ are the lumped spring stiffness values of the thin-film interconnect and inner in-plane actuator array and G_{ic} is a matrix projecting the additional spring force at the tip of the interconnect back to actuator locations.

In general, there is a good agreement between experimental and model results when nonidealities are taken into account. Angular rotation of the vertical actuator tip is closely matched to the model, although the initial curvature due to residual stress changes the associated tip displacements from the ideal case. Similarly, in-plane motions of the two lateral actuator arrays (x, y, and θ_z displacements) are very similar to experimental results, so long as the interconnect stiffness is accounted for in the design as fabricated. With the existing robot leg configuration, this means that substantial in-plane rotations can only be generated by one joint at a time, although both joints were shown to function. The total in-plane displacement of the foot was approximately 900 μm for a 4.5-mm-long leg.

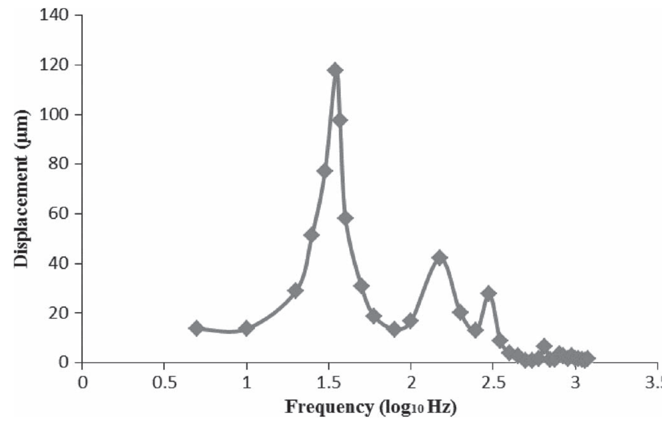

Fig. 11. Frequency response of point C (foot) measured with respect to global coordinates when the vertical actuator array is activated with driving sinusoidal input.

TABLE VI
RESONANT FREQUENCIES

Actuator	Measurement	1st and higher resonant frequency
Vertical actuator	Point A (hip)	300, 1500, 1810 Hz
	Point B (knee)	37, 300, 800 Hz
	Point C (foot)	35, 150, 300, 650 Hz
Compact actuator	Point A (hip)	1510, 1810 Hz
	Point B (knee)	800 Hz
	Point C (foot)	30, 150, 250, 650, 1150, 1450 Hz

D. Frequency Response

Resonance analysis of the fabricated m-DoF microrobotic legs indicates that such a robotic appendage is capable of moving under high bandwidth. Fig. 11 shows the frequency response of point C measured with respect to the global coordinate of high-speed camera under stereoscope when the vertical actuator array is activated with the driving sinusoidal input voltage where the offset and peak-to-peak voltages are chosen to 3 V and 2 Vpp, respectively. Q factor along the vertical motion is approximately obtained as 8.58 at the first resonant frequency of 34.7 Hz in a ten-base logarithm scale. Table VI shows resonant frequencies of other points when vertical actuator and compact actuator sets are independently activated. When the vertical actuator is activated, a 280-ms settling step time was observed at the foot.

E. Weight and Power Considerations

For use in producing terrestrial microrobot locomotion, weight bearing and energy use of a given robot leg design are critical. As fabricated, the primary source of out-of-plane compliance to load at the leg tip is the vertical actuators. This compliance can be estimated from (3), using an external moment on the vertical actuator equal to the weight load times the leg length. Estimated compliance is 3080 rad/N. For the actuated motion of the foot to be greater than any bending of the vertical actuators during load bearing, this produces an absolute maximum weight capacity of 2.1 mg per foot, which is somewhat further reduced by out-of-plane compliance of the lateral actuator arrays. Fortunately, each actuator array has a capacitance of only 1.2 nF, such that power consumption of three actuators at 15 V with a 15-Hz step frequency is only 12 μW. This would correspond to an approximate speed of 27 mm/s for the observed 0.9-mm step lengths of 15 steps/s from each leg. This translates to an ability to operate with battery power densities as low as 5.7 W/kg, well below that of current battery technologies. In practice, the ability to successfully operate a robot leg of this type with a power supply that it can carry is more dependent on the efficient use of energy in any control and energy conversion circuitry, than on its own fundamental power consumption [15].

Still, for the immediate development of microrobotic prototypes, the current work's primary benefits are the increased reliability of thin-film PZT actuator arrays and verification of actuator array modeling techniques. This process has produced a prototype hexapod using the leg design analyzed that has been produced with five out of six legs that are intact (one leg failing due to fracture of a flexure/tether unit during fabrication). Moving forward, however, more feasible robot prototypes for the next phase of further robot development will utilize millipede-style layouts, with larger numbers of legs, fewer actuators per leg, and shorter distances to leg tips to be explored. These prototypes thus trade reduced mobility for larger weight-bearing capacity (up to approximately 200 mg for an entire chassis) to allow greater flexibility in control and power systems. Nonetheless, the ability to create as complex leg geometries as described here while meeting fundamental needs for energy use versus weight-bearing capacity and the ability to predict leg behavior given fabrication constraints appear encouraging for a long-term goal of highly mobile bioinspired microscale robots.

V. Conclusion

Prototype microrobotic leg joint arrays based on thin-film piezoelectric actuation are described, fabricated, and characterized in this paper. These leg joints take advantage of high electric fields and good piezoelectric coefficients for thin-film PZT to generate large forces and/or joint angles from in-plane or out-of-plane motion. They are coupled with a robust fabrication process that allows multiple joints to be incorporated into full high-mobility legs. Modeling of thin-film PZT lateral and vertical actuator arrays is described, noting the benefits of having both free PZT unimorphs and thicker silicon structures in a combined structure. This integration is done with complex high-aspect-ratio silicon structures encapsulated by silicon dioxide vertical barrier trenches. Consistent undercut length of thin-film PZT actuator array is obtained with minimal effect on the piezoelectric performance of the actuators.

In experimental validation, both types of joint are shown to function in the integrated structure, with angular displacements varying from joint to joint. The in-plane motion generated by the final leg structure is smaller than the intended motion generated by the proposed m-DoF microrobotic leg due to the remaining silicon dioxide vertical barrier trenches. Nonetheless, performance is well predicted by microrobotic joint modeling that includes the following: 1) compensation for intrinsic residual stress of thin-film stacks that changes the initial deflection of the actuator arrays; 2) behavior of in-plane flexure joint array structures when the width of oxide trench barrier is taken into consideration; and 3) design of an electrical interconnect structure connected with the outer compact actuator array with less impact on the final device motion. Vertical actuation performed near-original design expectations ($\sim 40^\circ$) with only the neutral position changed by residual stress.

The completed leg structures permit faster leg movement with more degrees of freedom than previous walking microrobot actuators. Weight bearing is small but sufficient for the power demands of the piezoelectric actuators. Further improvement to the current design and fabrication of thin-film PZT devices will support continued microrobotic chassis development. This includes the parametric design of the stiffness of silicon flexure and tether in which the oxide vertical barrier trenches are taken into account, and the run-to-run stress analysis and process control of metal stack layers by which the initial out-of-plane bending of the appendage is minimized.

Appendix

Lateral Actuator Array Spring Definitions

From (4), the rotational spring stiffness values of the flexure, tether, and actuator are $k_{f,\theta}$, $k_{t,\theta}$, and $k_{\mathrm{act},\theta}$, respectively

$$k_{f,\theta} = \frac{(EI)_{\mathrm{flex}}}{L_{\mathrm{flex}}} \tag{11}$$

$$k_{t,\theta} = \frac{L_{\mathrm{act}}^2 (EA)_t}{L_t} \tag{12}$$

$$k_{\mathrm{act},\theta} = k_{\mathrm{act}}(F_{\mathrm{act}}) L_{\mathrm{act}}^2 \tag{13}$$

where k_{act} is the axial spring stiffness of the actuator dependent on the actuation force, $(EI)_{\mathrm{flex}}$ and $(EA)_t$ are the composite flexural rigidity values of the silicon and silicon dioxide flexure and tether along transverse and axial directions, respectively, L_{act} is the distance between the tether and the flexure joint, and L_{flex} and L_t are the lengths of the flexure joint and tether as shown in Fig. 1 and Table I. Because the actuator itself and the silicon tether experience the axial force generated by piezoelectric film, the maximum rotary angle is represented in terms of the combined spring stiffness of the joint structure in (11)–(13) as shown in Fig. 3.

Lateral Array Modifications for Interconnect Stiffness

When combining lateral actuator models, such as that defined by (4) and (11)–(13), basic equation (4) can be applied to the outer in-plane actuator array (joint γ), but in the m-DoF device fabricated, the motion of the inner lateral actuation array (joint β) is limited by the need to deliver an electrical signal to joint γ. This signal is transferred via an elastic interconnect created from the PZT–metal stack. As the inner compact array and the interconnect are mechanically connected in parallel, the following relation is used to predict in-plane motion of the resulting combination, based on the assumption that only small angular displacements contribute nonnegligible stiffness to the elastic interconnect:

$$M_{\mathrm{ic},z} = \frac{(EI)_{\mathrm{ic},z}}{L_{\mathrm{ic}}} \sum_{i=1}^{8} \left(\theta_{z,(\beta)}\right)_i \tag{14}$$

where $(EI)_{\mathrm{ic},z}$ and L_{ic} are the composite in-plane rigidity and effective length of the material stacked PZT thin-film interconnect and $M_{\mathrm{ic},z}$ is the moment applied at the interconnect by the inner compact actuators. The displacement of the tip of the elastic interconnect from the center of in-plane compact array δ_c is estimated from the length of the PZT interconnect and the sum of rotational displacements of each link $\Sigma(\theta_{z,(\beta)})_i$. Since the inner compact array and the PZT thin film are connected in parallel, the radius of rotation exerted by inner compact array is close to δ_c for the small displacement exerted by the parallel structure of the interconnect and inner compact array. The moment is equivalent to the force, which is the ratio of $M_{ic,z}$ to δ_c from the center of rotation, applied at the tip of eighth link of inner compact array. This force applied at eighth link f_{ic}^8 is then projected onto each flexure by f_{ic}^i at ith link in addition to the forcing component by individual actuators to form new forcing terms within the array

$$f_{\mathrm{ic}}^8 \approx \frac{M_{\mathrm{ic},z}}{\delta_c} \begin{bmatrix} \sin\left(\theta_{z,(\beta)}\right)_8 \\ \cos\left(\theta_{z,(\beta)}\right)_8 \\ 0 \end{bmatrix} \quad f_{\mathrm{ic}}^i \approx \frac{M_{\mathrm{ic},z}}{\delta_c} \begin{bmatrix} \sin\left(\theta_{z,(\beta)}\right)_{i,8} \\ \cos\left(\theta_{z,(\beta)}\right)_{i,8} \\ 0 \end{bmatrix} \tag{15}$$

where $\left(\theta_{z,(\beta)}\right)_{i,8}$ is the sum of rotational displacements from ith link to eighth link. Then, the forcing term $f_{(\beta)}^n$ in (5) consists of $[F_{\mathrm{act}}, 0, F_{\mathrm{act}}]^{\mathrm{T}}$ and f_{ic}^i, and the nonlinear system of equations from (5), (14), and (15) is solved numerically for $\left(\theta_{z,(\beta)}\right)_i$ [9].

From (10), the stiffness matrix $K_{\mathrm{ic,eq}}$ for PZT interconnect is modeled as

$$\begin{aligned} d_{\mathrm{ic}} = \begin{bmatrix} x_{\mathrm{ic}} \\ y_{\mathrm{ic}} \\ z_{\mathrm{ic}} \\ \theta_{\mathrm{ic},y} \\ \theta_{\mathrm{ic},z} \end{bmatrix} &= K_{\mathrm{ic.eq}}^{-1} F_{\mathrm{ic}} \\ &= \begin{bmatrix} L_{\mathrm{ic}}(EA)_{\mathrm{ic}}^{-1} & 0 & 0 \\ 0 & 0 & L_{\mathrm{ic}}^2\left(2(EI)_{\mathrm{ic},z}\right)^{-1} \\ 0 & -L_{\mathrm{ic}}^2\left(2(EI)_{\mathrm{ic},y}\right)^{-1} & 0 \\ 0 & L_{\mathrm{ic}}(EI)_{\mathrm{ic},y}^{-1} & 0 \\ 0 & 0 & L_{\mathrm{ic}}(EI)_{\mathrm{ic},z}^{-1} \end{bmatrix} \\ &\quad \times \begin{bmatrix} F_{\mathrm{ic},x} \\ M_{\mathrm{ic},y} \\ M_{\mathrm{ic},z} \end{bmatrix} \end{aligned} \tag{16}$$

where F_{ic} is the forcing term applied at the tip of the interconnect with the axial force $F_{\mathrm{ic},x}$, out-of-plane moment $M_{\mathrm{ic},y}$, and rotational moment $M_{\mathrm{ic},z}$, respectively. Then, the relation of the forcing term F_{ic} to the lateral actuation force F_{act} within joint β is obtained

$$\begin{aligned} F_{\mathrm{ic}} &= \begin{bmatrix} L_{\mathrm{act}}\delta_c^{-1}\cos\left(\sum_{i=1}^{8}\left(\theta_{z,(\beta)}\right)_i\right) \\ L_{\mathrm{act}}\varepsilon_{\mathrm{dist}}L_{\mathrm{ic}}^{-1}\delta_c^{-1}\cos\left(\sum_{i=1}^{8}\left(\theta_{z,(\beta)}\right)_i\right) \\ L_{\mathrm{act}} \end{bmatrix} N \cdot F_{\mathrm{act}} \\ &= G_{\mathrm{ic}} F_{\mathrm{act}}. \end{aligned} \tag{17}$$

A lumped compliance matrix for the joint β is derived for the case when only very small displacements of point B are observed and joint displacement is assumed to be exerted equally by each actuator. This model, combining the motions at the eight individual actuators into an approximate lumped model, becomes (18), shown at the bottom of the page.

ACKNOWLEDGMENT

The authors would like to thank Dr. P. Herrera-Fierro and T. Latowski for the assistance in chemical–mechanical polishing at Lurie Nanofabrication Facility of the University of Michigan, J. Martin and B. Power for metallization and milling at the U.S. Army Research Laboratories, and L. Sanchez for PZT deposition at Radiant Technologies, Inc.

$$\begin{aligned} d_{8(\beta)}^1 = \begin{bmatrix} x_{(\beta)} \\ y_{(\beta)} \\ z_{(\beta)} \\ \theta_{y,(\beta)} \\ \theta_{z,(\beta)} \end{bmatrix} &\approx K_{\mathrm{array,eq}}^{-1} F_{\mathrm{act}} \\ &= \begin{bmatrix} L_{\mathrm{flex}}(EA)_{\mathrm{flex}}^{-1} & 0 & 0 \\ 0 & 0 & L_{\mathrm{flex}}^2 L_{\mathrm{act}}\left(2(EI)_{\mathrm{flex,z}}\right)^{-1} \\ 0 & -L_{\mathrm{flex}}^2\left(2(EI)_{\mathrm{flex,y}}\right)^{-1} & 0 \\ 0 & L_{\mathrm{flex}}(EI)_{\mathrm{flex,y}}^{-1} & 0 \\ 0 & 0 & k_{\theta,\mathrm{tot}}^{-1} L_{\mathrm{act}} \end{bmatrix} N \cdot F_{\mathrm{act}} \end{aligned} \tag{18}$$

REFERENCES

[1] P. Dario, R. Valleggi, M. C. Carrozza, M. C. Montesi, and M. Cocco, "Microactuators for microrobots: A critical survey," *J. Micromech. Microeng.*, vol. 2, no. 3, pp. 141–157, Sep. 1992.

[2] T. Ebefors, J. U. Mattsson, E. Kälvesten, and G. Stemme, "A walking silicon micro-robot," in *Proc. TRANSDUCERS*, 1999, pp. 1202–1205.

[3] R. Murthy, A. Das, and D. O. Popa, "ARRIpede: An assembled micro crawler," in *Proc. IEEE Conf. Nanotechnol.*, 2008, pp. 833–836.

[4] S. Hollar, A. Flynn, C. Bellew, and K. S. J. Pister, "Solar powered 10 mg silicon robot," in *Proc. IEEE Int. Conf. MEMS*, 2003, pp. 706–711.

[5] S. Bergbreiter and K. S. J. Pister, "Design of an autonomous jumping microrobot," in *Proc. IEEE Int. Conf. Robot. Autom.*, 2007, pp. 447–453.

[6] B. R. Donald, C. G. Levey, and I. Paprotny, "Planar microassembly by parallel actuation of MEMS microrobots," *J. Microelectromech. Syst.*, vol. 17, no. 4, pp. 789–808, Aug. 2008.

[7] M. H. Mohebbi, M. L. Terry, K. F. Bohringer, G. T. A. Kovacs, and J. W. Suh, "Omni directional walking microrobot realized by thermal microactuator arrays," in *Proc. ASME Int. Mech. Eng. Congr. Expo.*, 2001, pp. 167–173.

[8] K. R. Oldham, J. S. Pulskamp, R. G. Polcawich, and M. Dubey, "Thin-film PZT lateral actuators with extended stroke," *J. Microelectromech. Syst.*, vol. 17, no. 4, pp. 890–899, Aug. 2008.

[9] K. R. Oldham, C. Rhee, J. Ryou, R. Polcawich, and J. Pulskamp, "Lateral thin-film piezoelectric actuators for bio-inspired micro-robotic locomotion," in *Proc. ASME Int. Conf. DETC*, 2009, vol. 6, pp. 759–768.

[10] B. Edamana, B. Hahn, J. S. Pulskamp, R. G. Polcawich, and K. R. Oldham, "Modeling and optimal low-power on-off control of thin-film piezoelectric rotational actuators," *IEEE/ASME Trans. Mechatronics*, vol. 16, no. 5, pp. 884–896, Oct. 2011.

[11] Z. Qiu, J. S. Pulskamp, X. Lin, C. Rhee, T. Wang, R. G. Polcawich, and K. R. Oldham, "Large displacement vertical translational actuator based on piezoelectric thin films," *J. Micromech. Microeng.*, vol. 20, no. 7, pp. 075016-1–075016-10, Jul. 2010.

[12] R. T. Howe and R. S. Muller, "Polycrystalline and amorphous silicon micromechanical beams: Annealing and mechanical properties," *Sens. Actuators*, vol. 4, no. 3, pp. 447–454, 1983.

[13] S. Trolier-Mckinstry and P. Muralt, "Thin film piezoelectrics for MEMS," *J. Electroceram.*, vol. 12, no. 1/2, pp. 7–17, 2004.

[14] R. Murthy and D. O. Popa, "A four degree of freedom microrobot with large work volume," in *Proc. IEEE Int. Conf. Robot. Autom.*, 2009, pp. 1028–1033.

[15] K. R. Oldham, B. Hahn, and P. Park, "On-off control for low-power servo control in piezoelectricmicro-robotics," in *Proc. ASME Dyn. Syst. Control Conf.*, 2008, pp. 1269–1276.

[16] P. Muralt, R. Polcawich, and S. Trolier-McKinstry, "Piezoelectric thin films for sensors, actuators, and energy harvesting," *MRS Bull.*, vol. 34, no. 9, pp. 658–664, Sep. 2009.

[17] N. J. Conway and S.-G. Kim, "Large-strain, piezoelectric, in-plane micro-actuator," in *Proc. IEEE Int. Conf. MEMS*, 2004, pp. 454–457.

[18] E. E. Aktakka, R. L. Peterson, and K. Najafi, "Multi-layer PZT stacking process for piezoelectric bimorph energy harvesters," in *Proc. Int. Workshop Micro Nanotechnol. Power Gener. Energy Convers. Appl.*, 2011, pp. 139–142.

[19] D. Campolo, M. Sitti, and R. S. Fearing, "Efficient charge recovery method for driving piezoelectric actuators with quasi-square waves," *IEEE Trans. Ultrason., Ferroelect., Freq. Control*, vol. 50, no. 3, pp. 237–244, Mar. 2003.

[20] H.-B. Fang, J.-Q. Liu, Z.-Y. Xu, L. Dong, L. Wang, D. Chen, B.-C. Cai, and Y. Liu, "Fabrication and performance of MEMS-based piezoelectric power generator for vibration energy harvesting," *Microelectron. J.*, vol. 37, no. 11, pp. 1280–1284, Nov. 2006.

[21] J. P. Pulskamp and R. G. Polcawich, "Negative vertical deflection piezoelectric MEMS actuators method of fabrication," U.S. Patent 7 944 121, May 17, 2011.

[22] J. P. Pulskamp and R. G. Polcawich, "Large force and displaement piezoelectric MEMS lateral actuator," U.S. Patent 7 876 026, Jan. 25, 2011.

Choong-Ho Rhee (S'10–M'11) received the B.S. degree in mechanical engineering from the University of California, Los Angeles, in 2005, and the M.S. and Ph.D. degrees in mechanical engineering from the University of Michigan, Ann Arbor, in 2009 and 2012, respectively.

He is currently a Postdoctoral Research Fellow with the Vibration and Acoustics Laboratory: Microsystems, University of Michigan. His research interests include robust parametric design, modeling, and microfabrication of MEMS devices, and bioinspired microrobotics.

Dr. Rhee is a member of the American Society of Mechanical Engineers (ASME).

Jeffrey S. Pulskamp received the B.S. degree in mechanical engineering from the University of Maryland, College Park, in 2000.

He is currently a MEMS Design and Mechanical Engineer with the Micro and Nano Materials and Devices Branch, U.S. Army Research Laboratory, Adelphi Laboratory Center, Adelphi, MD. His current research interests include RF MEMS devices, electromechanical design and modeling of MEMS, and millimeter-scale robotics. He is currently the holder of eight patents related to piezoelectric MEMS devices and has an additional five patents pending.

Ronald G. Polcawich (M'07) received the B.S. degree in materials science and engineering from Carnegie Mellon University, Pittsburgh, PA, in 1997, and the M.S. degree in materials and the Ph.D. degree in materials science and engineering from The Pennsylvania State University, University Park, in 1999 and 2007, respectively.

He is currently a Staff Researcher with the Micro and Nano Materials and Devices Branch, U.S. Army Research Laboratory, Adelphi Laboratory Center, Adelphi, MD, where he is also currently the Team Lead for the RF MEMS and millimeter-scale robotics programs. The current research programs include switches and phase shifters for phased array antennas, tunable MEMS resonators/filters for secure communication, and mobile unattended sensor platforms. His research activities include materials processing of lead zirconate titanate thin films, MEMS fabrication, piezoelectric MEMS, RF components, MEMS actuators, and millimeter-scale robotics. He is currently the holder of four patents and has authored over 30 journal articles, one book chapter on the fabrication and design of piezoelectric MEMS devices, and one book chapter on piezoelectric MEMS switches.

Dr. Polcawich is a member of the Ferroelectrics Committee of the IEEE Ultrasonics, Ferroelectrics, and Frequency Control Society. Additionally, he is a member of the American Ceramics Society.

Kenn R. Oldham (M'10) received the B.S. degree in mechanical engineering from Carnegie Mellon University, Pittsburgh, PA, in 2000, and the Ph.D. degree in mechanical engineering from the University of California, Berkeley, in 2006.

He is currently an Assistant Professor of mechanical engineering at the University of Michigan, Ann Arbor. His research interests include microsystem design and modeling, optimal design and control, and efficient sensing and power circuitry for MEMS devices.

Dr. Oldham is a member of the American Society of Mechanical Engineers (ASME) and the American Society for Engineering Education (ASEE).